APPLIED PHYSICS

Noninvasive measurement of local stress inside soft materials with programmed shear waves

Zhaoyi Zhang[1], Guo-Yang Li[2]*, Yuxuan Jiang[1], Yang Zheng[1], Artur L. Gower[3], Michel Destrade[4,5], Yanping Cao[1]*

Mechanical stresses across different length scales play a fundamental role in understanding biological systems' functions and engineering soft machines and devices. However, it is challenging to noninvasively probe local mechanical stresses in situ, particularly when the mechanical properties are unknown. We propose an acoustoelastic imaging–based method to infer the local stresses in soft materials by measuring the speeds of shear waves induced by custom-programmed acoustic radiation force. Using an ultrasound transducer to excite and track the shear waves remotely, we demonstrate the application of the method by imaging uniaxial and bending stresses in an isotropic hydrogel and the passive uniaxial stress in a skeletal muscle. These measurements were all done without the knowledge of the constitutive parameters of the materials. The experiments indicate that our method will find broad applications, ranging from health monitoring of soft structures and machines to diagnosing diseases that alter stresses in soft tissues.

INTRODUCTION

Mechanical stresses are important in biological and artificial soft materials across different length scales and play an essential role in their functions. For instance, adherent animal cells generate mechanical stress to migrate, divide, sense their environment, and communicate with other cells (*1*–*4*). At the tissue level, differential and/or constrained growth generates mechanical stresses that may trigger elastic instabilities and buckling patterns, leading to various morphological changes observed in nature (*5*–*7*). Forces produced by muscle contractions result in nearly all the movements in the human body (*8*–*10*). In short, it is fair to say that all living tissues are under mechanical stresses, even at rest, and understanding their distribution and magnitude is critical for uncovering the biophysics underpinning various life activities (*2*).

Stresses play a vital role also in artificial soft materials (*11*, *12*), which are used, for example, in designing soft machines and developing wearable and implantable soft bioelectronics. Residual and/or applied mechanical stresses cannot be avoided in these applications (*10*, *13*, *14*). Being able to probe the mechanical stress in situ is needed for the optimal design of soft machines/instruments and for the evaluation of their mechanical behavior, e.g., fatigue life (*15*, *16*).

To date, it remains a great challenge to probe the mechanical stresses of soft materials in situ in a noninvasive manner, especially when their mechanical properties are not known (*2*). Traditionally, stresses can be inferred from measured deformations (*10*, *17*), provided that the mechanical properties and the undeformed configuration of the tested material are known. The hole drilling method (*18*, *19*) is such an example that enables the measurement of residual stress destructively. Many nondestructive methods have been developed, including ones that use x-rays, neutron diffraction, and ultrasonic waves (*19*, *20*), but these all require prior knowledge of the material constants and the undeformed configurations of tested materials, all of which are challenging to acquire. For example, stress alters the speed of ultrasonic waves by the acoustoelastic effect (*19*, *21*–*23*). However, its interpretation requires knowledge of the third-order elastic constants, and calibrating for these parameters is by no means trivial, even in controlled laboratory environments (*21*, *22*, *24*, *25*).

Measuring the constitutive parameters of soft tissues in vivo or of artificial soft materials in service represents an even greater challenge. Moreover, the mechanical properties of these materials may vary with environment, time, and working state. Here, we propose a nondestructive method based on acoustoelasticity to measure stresses inside a soft material without invoking the prior knowledge of these constitutive parameters.

The acoustoelastic effect has previously been reported in soft materials; see, e.g., (*9*, *24*, *26*). Soft materials can undergo large elastic deformations when subject to mechanical stresses, which markedly alter the shear wave speeds (~100%) but barely change the speed of the longitudinal wave. That is because it only takes stresses in the kilopascal to deform soft solids, and typically, the latter speed (v_L, say) is such that ρv_L^2 (where ρ is the mass density) is in the order of gigapascal, while the former speed (v_T, say) is such that ρv_T^2 is in the order of kilopascal (*27*). Technically, the unaffected longitudinal (ultrasound) waves travel ~1000 times faster than shear waves. They provide a unique way to excite (by acoustic beam focusing) and visualize (by ultrasound imaging) shear waves remotely and locally.

In this method, we create a supershear moving load that remotely excites shear waves propagating along two orthogonal directions and measure their speeds with a frame rate of 10 kHz. We validate our method by successfully measuring uniaxial and bending stresses in a hydrogel sample and tensile stress in a skeletal muscle (which is intrinsically anisotropic due to the preferred direction of the aligned

[1]Institute of Biomechanics and Medical Engineering, AML, Department of Engineering Mechanics, Tsinghua University, Beijing 100084, P.R. China. [2]Harvard Medical School and Wellman Center for Photomedicine, Massachusetts General Hospital, Boston, MA 02139, USA. [3]Department of Mechanical Engineering, University of Sheffield, Sheffield, UK. [4]School of Mathematical and Statistical Sciences, University of Galway, Galway, Ireland. [5]Key Laboratory of Soft Machines and Smart Devices of Zhejiang Province and Department of Engineering Mechanics, Zhejiang University, Hangzhou 310027, Zhejiang Province, P.R. China.
*Corresponding author. Email: caoyanping@tsinghua.edu.cn (Y.C.); gli26@mgh.harvard.edu (G.-Y.L.)

muscle fibers). In these measurements of mechanical stresses, we do not need to know, or use, the constitutive parameters of the materials.

RESULTS

Measuring mechanical stresses with shear waves

Consider a plane shear wave with mechanical displacement $\boldsymbol{u} = \boldsymbol{u}_0 e^{ik(x_1\cos\theta + x_3\sin\theta - vt)}$ propagating in an incompressible soft solid subject to in-plane stresses σ_1 and σ_3 (see Fig. 1A), where $\boldsymbol{u}_0$ is the amplitude that lies in the propagation plane, v is the phase speed, t is the time, x_i (i = 1,2, and 3) is the Cartesian coordinate system aligned with the principal stress, and k is the wave number. The wave vector is $\boldsymbol{k} = k[\cos\theta, 0, \sin\theta]^T$, where k is the wave number and θ denotes the angle between $\boldsymbol{k}$ and the x_1 axis. The material can have any form of anisotropy, such as due to initial stress (*25*, *28*, *29*) or fibers reinforcing the solid (*30*), as long as they are aligned with the principal directions of the stress. In effect, for many tissues, structural anisotropy is coaxial with the stress, because collagen fibrils often act to optimize the load-bearing capacity (*31*–*33*). Inserting the plane wave form into the equations of acoustoelasticity, we get (see notes S1 and S2)

$$\rho v^2 = \alpha\cos^4\theta + 2\beta\cos^2\theta\sin^2\theta + \gamma\sin^4\theta \quad (1)$$

where $\alpha = \mathcal{A}^0_{1313}$, $2\beta = \mathcal{A}^0_{1111} + \mathcal{A}^0_{3333} - 2\mathcal{A}^0_{1133} - 2\mathcal{A}^0_{3113}$, $\gamma = \mathcal{A}^0_{3131}$, and $\mathcal{A}^0_{piqj}$ are the components of the Eulerian elastic moduli tensor.

Now consider two shear waves, traveling in two perpendicular directions $\theta = \theta_0$ and $\theta = \pi/2 + \theta_0$ with phase speeds v_x and v_z, respectively, where x and z denote a Cartesian coordinate system aligned with the main axes of the transducer (x, y, and z are the lateral, elevational, and axial directions, respectively).

We find that $\rho(v_x^2 - v_z^2) = (\alpha - \gamma)\cos(2\theta_0)$ according to Eq. 1 and that $\alpha - \gamma = \sigma_1 - \sigma_3$, regardless of the constitutive model and out-of-plane stress (see notes S1 and S2). Taking the two equations together, we conclude that

$$\sigma_1 - \sigma_3 = \rho\frac{v_x^2 - v_z^2}{\cos 2\theta_0} \quad (2)$$

which is the foundation of our method to measure mechanical stresses in soft materials. For the case of uniaxial stress ($\sigma_3 = 0$), Eq. 2 gives direct access to σ_1. While Eq. 2 holds for any θ_0, we find that $\theta_0 = 0$ is the best choice for practical measurements. First is because $\theta_0 = 0$ gives the best sensitivity to the stress when the speeds are measured. Second is because it is simpler to measure the group speed $\boldsymbol{v}_g \equiv \partial(kv)/\partial\boldsymbol{k}$ with ultrasound shear wave elastography (*34*) than the phase speed v in Eq. 2 and these two speeds are the same along the principal directions (see fig. S1), which is the case here when $\theta_0 = 0$ (Fig. 1B). See note S2 for more details.

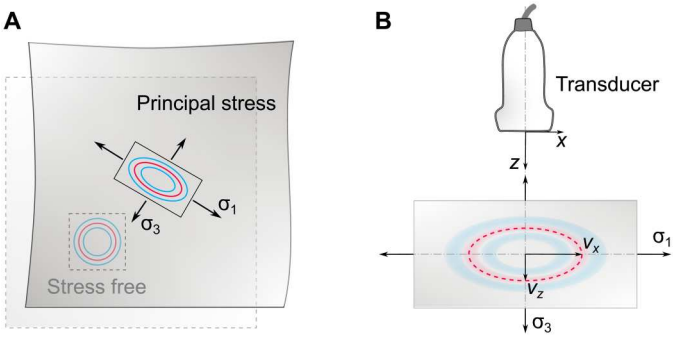

Fig. 1. Principle of acoustoelastic imaging of stresses. (**A**) Schematic showing that the principal stresses σ_1 and σ_3 change the speed of the vertically polarized shear waves. Here, an isotropic material subject to moderate stress is taken as an example. (**B**) An ultrasonic transducer with the axial direction (z) aligned with the principal direction x_3 is used to measure the wave speeds v_x and v_z along the two principal directions. The principal stresses are connected to the two shear wave speeds.

Generating shear waves propagating in perpendicular directions with programmed acoustic radiation force

Our experimental setup to generate two shear waves propagating perpendicularly to each other, shown in Fig. 2A, was based on a medical ultrasound imaging system (see Materials and Methods). The ultrasound transducer sent 7-MHz ultrasound waves that were used to excite and detect shear waves in soft materials. In effect, the absorption of the ultrasound waves leads to a transfer of momentum to the soft materials, giving rise to the acoustic radiation force (ARF). A focused ultrasound beam can deliver the ARF locally, resulting in a Gaussian-shaped body force at the focus (see fig. S2B). Micrometer amplitude shear waves traveling perpendicular to the ultrasound beam (x axis) are then generated by the ARF, and measuring their speed enables what is called shear wave elastography (*35*, *36*). However, with a standard setup, shear waves traveling along the beam direction (z axis) are not easily detectable, because they are small and attenuate rapidly (see movies S1B and S2B for simulation and experimental results, respectively) (*37*).

To excite the laterally and vertically propagated shear waves simultaneously, we present a previously unreported programming method that successively focuses the ultrasound beam at six locations (the duration at each location is ~43 μs), separated by a distance of d = 1 mm, along the lateral direction x, as shown in Fig. 2A. These ARFs mimic a laterally moving load with a supershear wave speed (the ratio of the moving speed and the shear wave speed, i.e., the Mach number, is ~10). The shear waves generated by the moving load mutually interfere following the Huygens-Fresnel principle, which significantly enlarges the amplitude of the vertical wave. The vertically propagated shear waves are primarily vertically polarized. They are often called longitudinal shear waves, and have been used in ultrasound elastography of the liver for example (*38*, *39*). Approximately 0.3 ms after the wave excitation, unfocused ultrasound beams are sent by the same ultrasound transducer to perform ultrafast ultrasound imaging (*40*), which records the shear wave propagation in the region of interest (ROI) at a rate of 10,000 frames per second.

We tested our experimental setup on a polyvinyl alcohol (PVA) hydrogel (mass density of $\rho \sim 1$ g/cm^3 and initial shear modulus of ~8.6 kPa; see Materials and Methods). The approximate size is 29 by 6 cm^2 cross section and 4 cm in depth (Fig. 2C). Figure 2D depicts the snapshots of the shear wave propagation in the sample and shows that the shear waves propagated in lateral and vertical

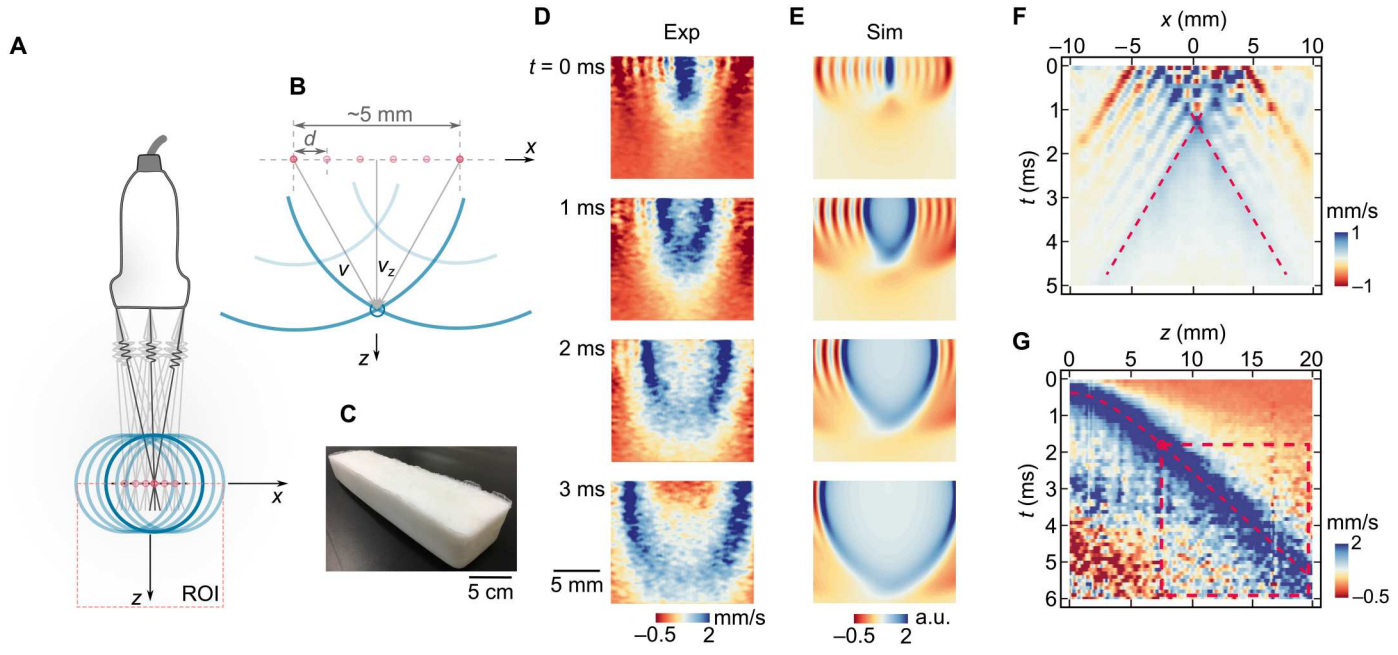

Fig. 2. Acoustoelastic imaging using ultrasound shear wave elastography. (**A**) Schematic of the experimental setup. An ultrasound beam focuses successively from left to right along the *x* axis at six locations inside the material separated by distance $d = 1$ mm to excite multiple shear waves. Interference of the shear waves gives rise to a strong vertically propagated shear wave (along the *z* axis). Wave propagation in the region of interest (ROI) is measured by plane wave ultrasound imaging. (**B**) Schematic showing the propagation of the interference at $(2.5d, z)$, with a speed of $\left[z/\sqrt{z^2+(2.5d)^2}\right]v$. (**C**) Photograph of the hydrogel sample at rest. (**D**) Snapshots showing the shear wave propagation in the ROI. The maps depict the vertical particle velocity fields. Exp, experiment. (**E**) Finite element simulations of the shear wave propagation. a.u., arbitrary units; Sim, simulation. (**F** and **G**) Spatiotemporal maps of the laterally (along *x*) and vertically propagated (along *z*) shear waves. (**G**) shows that the shear wave speed is constant only when the shear wave propagates far away ($z > 7$ mm, the dashed square), in line with the theoretical prediction $\left[z/\sqrt{z^2+(2.5d)^2}\right]v \to v_z$ for large *z*. The shear wave speeds v_x and v_z are measured from (F) and (G), respectively, by the Radon transformations (see fig. S4).

directions are generated simultaneously, in excellent agreement with the finite element simulations (see Materials and Methods) shown in Fig. 2E and movie S1A. For anisotropic materials, we also performed three-dimensional (3D) finite element simulations to confirm that vertically propagated shear waves are primarily excited using our programmed ARFs and that the shear waves travelling in lateral and vertical directions are generated simultaneously (see fig. S3).

To measure the shear wave speeds, we extract the spatiotemporal data along the lateral (*x* axis) and vertical (*z* axis) directions, respectively. As shown in Fig. 2F, six shear waves propagate to the left and to the right, with a linear wavefront that suggests that the wave speed v_x is constant. However, the vertically propagated waves gradually decelerate from the near field to the far field (Fig. 2G), with the measured speed v_z approximately following $\frac{z}{\sqrt{z^2+(2.5d)^2}}v$, where v is the shear wave speed along $\theta = \tan^{-1}\left(\frac{z}{2.5d}\right)$. This is expected and is likely due to the wave interference pattern depicted in Fig. 2B. Note that for large enough z, we have $\frac{z}{\sqrt{z^2+(2.5d)^2}}v \sim v$ and v should be the speed of the vertically propagated shear wave that we want to measure. For this reason, we only use the data for $z >$ 7 mm (the dashed square in Fig. 2G) in the subsequent analysis.

To derive the group velocities in a robust way, we apply the Radon transformation (*41*) to the spatiotemporal data shown in Fig. 2 (F and G) to compute v_x and v_z (for the lateral direction *x*, a directional filter is performed to the spatiotemporal data before the Radon transformation; see note S3 and fig. S4). In the absence of mechanical stress, we get $v_x = 2.81 \pm 0.05$ m/s and $v_z = 2.82 \pm 0.06$ m/s, which agrees with the theoretical prediction that $v_x = v_z$ in the absence of mechanical stress. The initial shear modulus derived from the shear wave speeds is $\mu = 8.46 \pm 0.33$ kPa, in agreement with the mechanical characterization performed by indentation tests (shear modulus 8.6 ± 0.3 kPa; see note S4).

Measuring stresses in hydrogel and muscle without the knowledge of their constitutive parameters

For our first test, to demonstrate the usefulness of our theory and method, we applied uniaxial stress to the hydrogel sample σ_1 along the *x* direction and then measured v_x and v_z. As shown in Fig. 3A, the tensile/compressive stress increases/decreases v_x but decreases/increases v_z. The identified stress shows a good agreement with the applied stress, with a maximum error of ~5% (Fig. 3B).

Furthermore, we measured the stress induced by the bending deformation of the hydrogel sample. As shown in Fig. 3C, we applied a 4-cm deflection to bend the sample, which resulted in an approximately linear stress field across the thickness of the sample (see the simulation in Fig. 3C). We perform measurements within four planes parallel to the neutral plane of zero stress, at $y = -20$, −14.7,12.8, and 20 mm. Figure 3D shows the stresses measured at

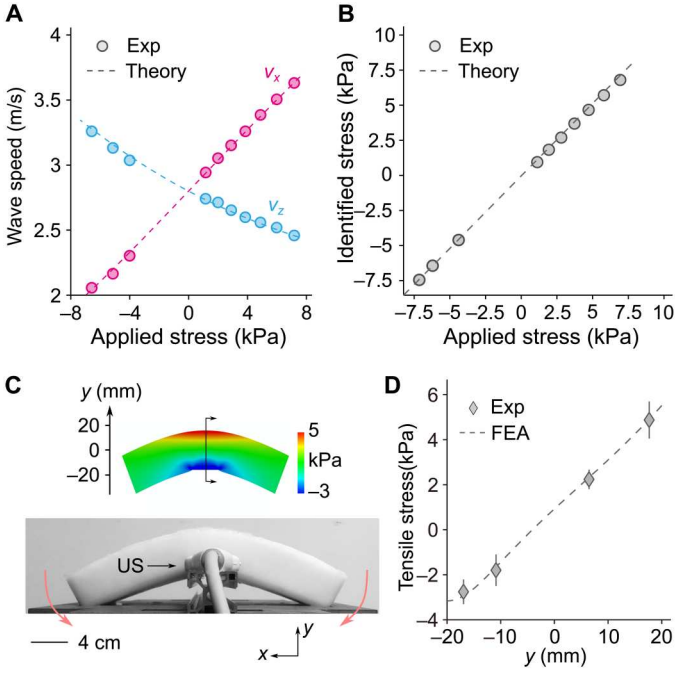

Fig. 3. Acoustoelastic imaging of a soft material. (**A**) Shear wave speeds measured in a hydrogel subject to a uniaxial stress. (**B**) Comparison of identified stress with the applied stress. Dashed line represents the 45° line for visual guide. (**C**) Photograph showing the sample under bending deformation and finite element computation of the bending stress. US, ultrasonic transducer. (**D**) Bending stress is measured by acoustoelastic imaging and in comparison with theory. Error bars denote the SDs of five measurements. FEA, finite element analysis.

different locations, which agree with the theoretical values obtained using finite element simulations.

We proceed to demonstrate the effectiveness of our method in probing the mechanical stresses in anisotropic soft tissues. To this end, we performed ex vivo measurements on a sample of porcine skeletal muscle, as shown in Fig. 4A. The elastic deformation of the skeletal muscle can be captured using a transversely isotropic model reflecting the preferential orientation of the muscle fibers, as shown by the ultrasound brightness mode (B-mode) image (Fig. 4B). In this experiment, we applied tensile stress along the muscle fibers using several weights (each weight is ~500 g), mimicking a passive stretch of the skeletal muscle (*42*). Figure 4C shows a representative snapshot (~2.6 ms after the AFRs push) of the shear wave propagation, when the applied stress is ~3.6 kPa. The ARFs are applied on the left side of the ROI, and then v_x is measured for the shear wave propagating from left to right. Compared with the hydrogel, it is apparent that the wavefronts are broader because of a larger shear wave speed and that there is a stronger dissipation (see note S5 for mechanical characterization of the skeletal muscle).

Figure 4D shows the velocities v_x and v_z obtained when the muscle is subject to different levels of mechanical stresses. The measurement uncertainties on the wave speeds are larger compared with the measurements on the hydrogel sample due to the broader wavefronts. As expected, intuitively, the wave speed v_x along the tension/fiber direction increases with the tensile stress. Notably, the shear wave speed v_z in the skeletal muscle increases with tension along x, in contrast to the isotropic hydrogel where v_z decreases. This is likely due to the nonlinear elastic response of the skeletal muscle, which makes it stiffer when increasing the tension (*43*, *44*). In the analysis, we find that a phenomenological model incorporating exponentially stiffening effects (see note S5) fits the experimental data, as shown in Fig. 4D.

The nontrivial acoustoelastic properties of the muscle again highlight the key advantage of our acoustoelastic imaging method: No acoustoelastic parameters of the materials were needed to predict the stress. We simply derive the tensile stresses from the shear wave speeds, as shown in Fig. 4E. The stress identified by our method shows a good agreement (maximum error of ~15%) with the applied stress. We attribute the larger error to the viscoelasticity of the biological sample.

DISCUSSION

On the basis of the acoustoelastic principle, we proposed a theory and a method to probe mechanical stresses in soft materials without prior knowledge of their constitutive parameters, in contrast to the existing methods presented to date. A key step to realizing our method was to program multiple ARFs to mimic a supershear moving load, generating shear waves in two mutually perpendicular directions. We were then able to obtain the speeds of both waves by ultrasonic imaging, which, according to our theory, allowed us to measure the mechanical stresses remotely. Hence, we successfully measured the spatial variation of bending stress in a hydrogel and of tensile stress in a passively stretched muscle, which is intrinsically anisotropic. The stretched muscle test illustrates how our method

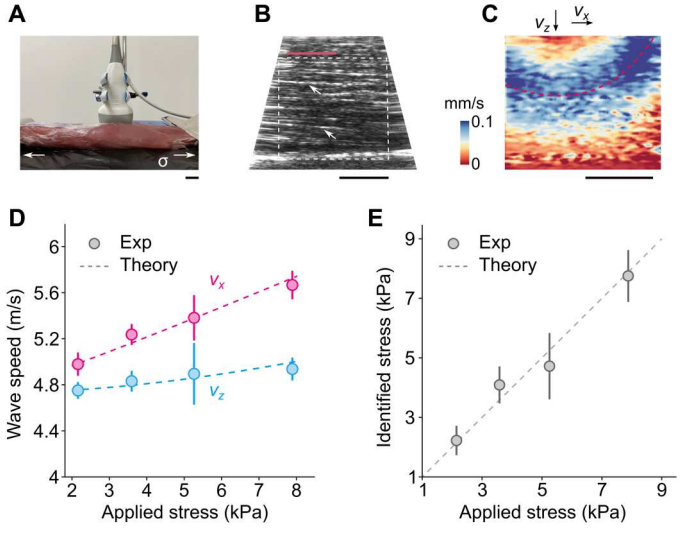

Fig. 4. Acoustoelastic imaging of a skeletal muscle. (**A**) Photograph of the skeletal muscle. (**B**) Grayscale B-mode image of the sample. In this view, the muscle fibers (some are indicated by the arrows) and the applied stress are along the horizontal direction. The acoustic radiation forces (ARFs) are applied along the red line. Dashed square represents the ROI where the wave speeds are measured. (**C**) A representative snapshot (~2.6 ms after ARFs push) of the wave propagation when the applied stress is ~3.6 kPa. Scale bars, 1 cm (A to C). (**D**) Shear wave speeds measured at different levels of stress. Markers, experiment. Error bar denotes the SDs of five measurements. Dashed lines represent theoretical curves that are obtained using a phenomenological model (see note S5). (**E**) Comparison between applied stress and identified stress. Dashed line represents the 45° line for visual guide.

works even in the presence of structural anisotropy when it is aligned with the stress. Our method relies on the measurement of vertically polarized shear waves in specific imaging orientations relative to the material axis of symmetry. When such an experimental setup is not achievable in an in vivo measurement, further efforts such as using 3D rotational imaging (*45*) or 3D ultrasonic transducer are needed to ensure that these waves can be excited and measured to infer the mechanical stress.

The effect of the viscoelasticity of soft materials on the proposed method deserves a careful discussion. As indicated by our experiments on skeletal muscle, inaccuracies may appear when neglecting viscosity. For high enough frequencies, biological tissues exhibit frequency-dependent responses due to viscosity, which, in turn, may affect the predictions of our method. To address this issue, we invoke the quasi-linear viscoelasticity theory, which models the stress relaxation with a Prony series, $\mu(t) = \mu_0[1 - \sum_{i=1}^{n} g_i(1 - e^{-t/\tau_i})]$, where $\mu(t)$ is the relaxation shear modulus in response to a step constant strain, μ_0 is the instantaneous shear modulus, τ_i is a characteristic relaxation time, and g_i is a dimensionless relaxation modulus (i = 1,2, ..., n). For simplicity, we take n = 1 and find that this model fits well the viscoelastic dispersion of shear waves in skeletal muscle over the 100- to 500-Hz range, with g_1 = 0.79 and τ_1 = 0.49 ms (see fig. S6E). We then use this model to evaluate the effect of viscoelasticity on the identified mechanical stresses based on a recently proposed acousto-viscoelastic theory (*46*). The results show that, over a broad frequency range (10 to 1000 Hz), the stress is underestimated when viscoelasticity comes into play (see note S5 and fig. S7). However, in our method, we use the group velocity of the shear waves (4-dB bandwidth from 100 to 1000 Hz; see fig. S8), and the average error over the frequency band is ~16%, consistent with our measurements. For soft materials where the extent of stress relaxation is less than ~50%, which covers a wide range of soft materials including most hydrogels and soft tissues, our analysis indicates that shear wave dispersion caused by viscosity has a negligible effect on mechanical stresses measured with the reported acoustoelastic imaging method (the maximum error is less than 10%).

Measuring the constitutive parameters of a soft material in situ is challenging, because the parameters change with time, environment, and from one working state to another. By bypassing this difficulty, our constitutive parameter-free theory and method to probe mechanical stresses in a nondestructive manner should find broad applications across different disciplines including, but not limited to, biomedical engineering, biology, medicine, materials science, and soft matter physics.

MATERIALS AND METHODS

Ultrasound setup

Our ultrasound experimental system was built on the Vantage 64 LE system (Verasonics Inc., Kirkland WA, USA). The central frequency, pitch, and element number of the ultrasound transducer (L9-4, JiaRui Electronics Technology Co., Shenzhen, China) used in our experiments were 7 MHz, 0.3 mm, and 128, respectively. The imaging sequence of the ultrasound experiment is depicted in fig. S2A. In the excitation stage, the focused ultrasound beams were generated by 32 elements (with a voltage of ~10 V, aperture size of ~10 mm, and uniform apodization). The focus was ~13 mm away from the transducer. In the imaging stage, while all the 128 elements (with a voltage of ~10 V, aperture size of ~40 mm, and uniform apodization) were used to transmit unfocused ultrasound beams, only the 64 elements at the center of the transducer were used as receivers. The ultrasound in-phase and quadrature signals during the wave propagation were acquired at a frame rate of 10 kHz. The plane wave imaging with delay and sum beamforming was adopted to reconstruct each frame (*47*). The particle velocity field was calculated offline based on the Loupas′ estimator (*48*) using a kernel size of 5 by 2 (0.275 mm in x and 0.2 ms in t). A spatial filter (mean filter) with a kernel size of 8 by 8 (0.87 mm in x and 0.44 mm in z) was then used to reduce the noise of the particle velocity. For all the experiments, 10 successive measurements (~56 ms) were performed, and the average of the measurements was taken to improve the signal-to-noise ratio.

Hydrogel phantom preparation

The hydrogel consisted of 10% PVA, 3% cellulose, and 87% deionized water by weights. We dissolved the PVA powder (Sigma-Aldrich, 341584, Shanghai, China) into 80°C water. We then added cellulose powder (Sigma-Aldrich, S3504, Shanghai, China) into the solution and fully stirred the solution to get a suspension of the cellulose powder. The cellulose particles act as ultrasonic scatterers to enhance the imaging contrast. We poured the suspension into a square plastic box (with a length of ~30 cm, width of ~7 cm, and height of ~4 cm) and then cooled the suspension to room temperature (~20°C) before putting it into a −20°C freezer. We froze the sample for 12 hours and then thawed it at room temperature for another 12 hours. The stiffness of the sample can be tuned by freezing/thawing (F/W) cycles (*49*). The hydrogel sample used in this study underwent two F/W cycles. We performed indentation tests on the hydrogel and measured the dispersion relation of the Rayleigh surface waves to characterize its elastic and viscoelastic properties (see note S4 and fig. S5).

Finite element analysis

The finite element analyses (FEA) were performed using Abaqus (Abaqus 6.14, Dassault Systèmes). We built a plane strain model with Abaqus/Standard for the shear wave generation in isotropic materials. The size of the model was 50 by 50 mm ^{2}. The ARF was modeled as a body force with a Gaussian shape of the form

$$\boldsymbol{f} = \boldsymbol{f}_0 \exp\left\{-\frac{[x - x^{(i)}]^2}{2r_x^2} - \frac{[z - z^{(i)}]^2}{2r_z^2}\right\} \quad (3)$$

where $\boldsymbol{f}_0$ is the magnitude of the force, with a direction parallel to the ultrasound beam and magnitude small enough to generate small-amplitude waves, and $[x^{(i)}, z^{(i)}]$ (i = 1,2, ...,6) are the coordinates of the six focal points. We took r_x = 0.5 mm (see fig. S2, B and C) and r_z = 1.0 mm. We used a uniform mesh grid (element size of 0.1 mm) and the CPE8RH element (plane strain, eight-node biquadratic, reduced integration, hybrid with linear pressure). Other parameters used in the simulations and the postanalyses were consistent with our experimental setup.

To check that our programmed ARFs generates vertically propagated waves, we built a 3D model with Abaqus/explicit. We used a geometry that was similar to the plane model for isotropic materials but extended the model thickness to 20 mm along the elevational direction (y axis). The Gaussian radius of the ARF along the y

axis is $r_y = r_x$. We used the C3D8 (eight-node linear brick, hybrid with constant pressure) element in the simulation, and the average mesh size for the 3D model was about 0.1 by 0.1 by 0.1 mm.

In the FEA of the bending stress, we built a plane stress model that was 30 cm long and 4 cm wide. The size of the model was consistent with our physical sample. We fixed the sample's lower left and right corners and prescribed the displacement (6 cm) at the middle of the lower boundary. We used a uniform mesh (0.5 cm) and the CPS8R element (plane stress, eight-node biquadratic, reduced integration).

Supplementary Materials

This PDF file includes:
Supplementary notes S1 to S5
Figs. S1 to S8
Legends for movies S1 and S2
References

Other Supplementary Material for this manuscript includes the following:
Movies S1 and S2

REFERENCES AND NOTES

1. N. L. Nerurkar, C. Lee, L. Mahadevan, C. J. Tabin, Molecular control of macroscopic forces drives formation of the vertebrate hindgut. *Nature* **565**, 480–484 (2019).
2. M. Gómez-González, E. Latorre, M. Arroyo, X. Trepat, Measuring mechanical stress in living tissues. *Nat. Rev. Phys.* **2**, 300–317 (2020).
3. K. H. Vining, D. J. Mooney, Mechanical forces direct stem cell behaviour in development and regeneration. *Nat. Rev. Mol. Cell Biol.* **18**, 728–742 (2017).
4. H. Ucar, S. Watanabe, J. Noguchi, Y. Morimoto, Y. Iino, S. Yagishita, N. Takahashi, H. Kasai, Mechanical actions of dendritic-spine enlargement on presynaptic exocytosis. *Nature* **600**, 686–689 (2021).
5. T. Tallinen, J. Y. Chung, F. Rousseau, N. Girard, J. Lefèvre, L. Mahadevan, On the growth and form of cortical convolutions. *Nat. Phys.* **12**, 588–593 (2016).
6. J.-H. Lee, H. S. Park, D. P. Holmes, Elastic instabilities govern the morphogenesis of the optic cup. *Phys. Rev. Lett.* **127**, 138102 (2021).
7. B. Li, F. Jia, Y.-P. Cao, X.-Q. Feng, H. Gao, Surface wrinkling patterns on a core-shell soft sphere. *Phys. Rev. Lett.* **106**, 234301 (2011).
8. S. K. Powers, M. J. Jackson, Exercise-induced oxidative stress: Cellular mechanisms and impact on muscle force production. *Physiol. Rev.* **88**, 1243–1276 (2008).
9. J. A. Martin, S. C. Brandon, E. M. Keuler, J. R. Hermus, A. C. Ehlers, D. J. Segalman, M. S. Allen, D. G. Thelen, Gauging force by tapping tendons. *Nat. Commun.* **9**, 1592 (2018).
10. J. Lee, S. J. Ihle, G. S. Pellegrino, H. Kim, J. Yea, C. Y. Jeon, H. C. Son, C. Jin, D. Eberli, F. Schmid, B. L. Zambrano, A. F. Renz, C. Forró, H. Choi, K. I. Jang, R. Küng, J. Vörös, Stretchable and suturable fibre sensors for wireless monitoring of connective tissue strain. *Nat. Electron.* **4**, 291–301 (2021).
11. J. Y. Sun, X. Zhao, W. R. Illeperuma, O. Chaudhuri, K. H. Oh, D. J. Mooney, J. J. Vlassak, Z. Suo, Highly stretchable and tough hydrogels. *Nature* **489**, 133–136 (2012).
12. J. Kim, G. Zhang, M. Shi, Z. Suo, Fracture, fatigue, and friction of polymers in which entanglements greatly outnumber cross-links. *Science* **374**, 212–216 (2021).
13. N. Matsuhisa, S. Niu, S. J. K. O'Neill, J. Kang, Y. Ochiai, T. Katsumata, H.-C. Wu, M. Ashizawa, G.-J. N. Wang, D. Zhong, X. Wang, X. Gong, R. Ning, H. Gong, I. You, Y. Zheng, Z. Zhang, J. B.-H. Tok, X. Chen, Z. Bao, High-frequency and intrinsically stretchable polymer diodes. *Nature* **600**, 246–252 (2021).
14. G. H. Lee, H. Moon, H. Kim, G. H. Lee, W. Kwon, S. Yoo, D. Myung, S. H. Yun, Z. Bao, S. K. Hahn, Multifunctional materials for implantable and wearable photonic healthcare devices. *Nat. Rev. Mater.* **5**, 149–165 (2020).
15. R. Bai, J. Yang, Z. Suo, Fatigue of hydrogels. *Eur. J. Mech. A/Solids* **74**, 337–370 (2019).
16. J. A. Rogers, T. Someya, Y. Huang, Materials and mechanics for stretchable electronics. *Science* **327**, 1603–1607 (2010).
17. Y. Wang, S. Lee, T. Yokota, H. Wang, Z. Jiang, J. Wang, M. Koizumi, T. Someya, A durable nanomesh on-skin strain gauge for natural skin motion monitoring with minimum mechanical constraints. *Sci. Adv.* **6**, eabb7043 (2020).
18. G. S. Schajer, Hole-drilling residual stress measurements at 75: Origins, advances, opportunities. *Exp. Mech.* **50**, 245–253 (2009).
19. N. S. Rossini, M. Dassisti, K. Y. Benyounis, A. G. Olabi, Methods of measuring residual stresses in components. *Mater. Des.* **35**, 572–588 (2012).
20. C. O. Ruud, A review of selected non-destructive methods for residual stress measurement. *NDT Int.* **15**, 15–23 (1982).
21. D. S. Hughes, J. L. Kelly, Second-order elastic deformation of solids. *Phys. Rev.* **92**, 1145 (1953).
22. A. N. Guz, F. G. Makhort, The physical fundamentals of the ultrasonic nondestructive stress analysis of solids. *Int. Appl. Mech.* **36**, 1119–1149 (2000).
23. F. Shi, J. E. Michaels, S. J. Lee, In situ estimation of applied biaxial loads with Lamb waves. *J. Acoust. Soc. Am.* **133**, 677–687 (2013).
24. J.-L. Gennisson, M. Rénier, S. Catheline, C. Barrière, J. Bercoff, M. Tanter, M. Fink, Acoustoelasticity in soft solids: Assessment of the nonlinear shear modulus with the acoustic radiation force. *J. Acoust. Soc. Am.* **122**, 3211–3219 (2007).
25. G.-Y. Li, A. Gower, M. Destrade, An ultrasonic method to measure stress without calibration: The angled shear wave method. *J. Acoust. Soc. Am.* **148**, 3963 (2020).
26. Y. Jiang, G. Y. Li, L. X. Qian, X. D. Hu, D. Liu, S. Liang, Y. Cao, Characterization of the nonlinear elastic properties of soft tissues using the supersonic shear imaging (SSI) technique: Inverse method, ex vivo and in vivo experiments. *Med. Image Anal.* **20**, 97–111 (2015).
27. C. Creton, C. Matteo, Fracture and adhesion of soft materials: A review. *Rep. Prog. Phys.* **79**, 046601 (2016).
28. M. Shams, M. Destrade, R. W. Ogden, Initial stresses in elastic solids: Constitutive laws and acoustoelasticity. *Wave Motion* **48**, 552–567 (2011).
29. A. L. Gower, T. Shearer, P. Ciarletta, A new restriction for initially stressed elastic solids. *Q. J. Mech. Appl. Math.* **70**, 455–478 (2017).
30. M. Destrade, M. D. Gilchrist, R. W. Ogden, Third-and fourth-order elasticities of biological soft tissues. *J. Acoust. Soc. Am.* **127**, 2103–2109 (2010).
31. C. Deroy, M. Destrade, A. Mc Alinden, A. Ní Annaidh, Non-invasive evaluation of skin tension lines with elastic waves. *Skin Res. Technol.* **23**, 326–335 (2017).
32. I. Hariton, G. Debotton, T. C. Gasser, G. A. Holzapfel, Stress-driven collagen fiber remodeling in arterial walls. *Biomech. Model. Mechanobiol.* **6**, 163–175 (2007).
33. G. W. Jones, S. J. Chapman, Modeling growth in biological materials. *SIAM Rev.* **54**, 52–118 (2012).
34. N. C. Rouze, A. Caenen, K. R. Nightingale, Phase and group velocities for shear wave propagation in an incompressible, hyperelastic material with uniaxial stretch. *Phys. Med. Biol.* **67**, 095015 (2022).
35. J. Bercoff, M. Tanter, M. Fink, Supersonic shear imaging: A new technique for soft tissue elasticity mapping. *IEEE Trans. Ultrason. Ferroelectr. Freq. Control* **51**, 396–409 (2004).
36. A. P. Sarvazyan, O. V. Rudenko, S. D. Swanson, J. B. Fowlkes, S. Y. Emelianov, Shear wave elasticity imaging: A new ultrasonic technology of medical diagnostics. *Ultrasound Med. Biol.* **24**, 1419–1435 (1998).
37. S. Catheline, N. Benech, Longitudinal shear wave and transverse dilatational wave in solids. *J. Acoust. Soc. Am.* **137**, EL200–EL205 (2015).
38. L. Sandrin, M. Tanter, J.-L. Gennisson, S. Catheline, M. Fink, Shear elasticity probe for soft tissues with 1-d transient elastography. *IEEE Trans. Ultrason. Ferroelectr. Freq. Control* **49**, 436–446 (2002).
39. L. Sandrin, D. Cassereau, M. Fink, The role of the coupling term in transient elastography. *J. Acoust. Soc. Am.* **115**, 73–83 (2004).
40. M. Tanter, M. Fink, Ultrafast imaging in biomedical ultrasound. *IEEE Trans. Ultrason. Ferroelectr. Freq. Control* **61**, 102–119 (2014).
41. N. C. Rouze, M. H. Wang, M. L. Palmeri, K. R. Nightingale, Robust estimation of time-of-flight shear wave speed using a radon sum transformation. *IEEE Trans. Ultrason. Ferroelectr. Freq. Control* **57**, 2662–2670 (2010).
42. J. P. Kerris, A. C. Betik, J. Li, G. K. McConell, Passive stretch regulates skeletal muscle glucose uptake independent of nitric oxide synthase. *J. Appl. Physiol.* **126**, 239–245 (2019).
43. B. Calvo, A. Ramírez, A. Alonso, J. Grasa, F. Soteras, R. Osta, M. J. Muñoz, Passive nonlinear elastic behaviour of skeletal muscle: Experimental results and model formulation. *J. Biomech.* **43**, 318–325 (2010).
44. J. P. Remeniéras, M. Bulot, J. L. Gennisson, F. Patat, M. Destrade, G. Bacle, Acousto-elasticity of transversely isotropic incompressible soft tissues: Characterization of skeletal striated muscle. *Phys. Med. Biol.* **66**, 145009 (2021).
45. A. E. Knight, C. A. Trutna, N. C. Rouze, L. D. Hobson-Webb, A. Caenen, F. Q. Jin, M. L. Palmeri, K. R. Nightingale, Full characterization of in vivo muscle as an elastic, incompressible, transversely isotropic material using ultrasonic rotational 3D shear wave elasticity imaging. *IEEE Trans. Med. Imag.* **41**, 133–144 (2021).
46. H. Berjamin, R. De Pascalis, Acoustoelastic analysis of soft viscoelastic solids with application to pre-stressed phononic crystals. *Int. J. Solids Struct.* **241**, 111529 (2022).

47. G. Montaldo, M. Tanter, J. Bercoff, N. Benech, M. Fink, Coherent plane-wave compounding for very high frame rate ultrasonography and transient elastography. *IEEE Trans. Ultrason. Ferroelectr. Freq. Control* **56**, 489–506 (2009).
48. T. Loupas, J. Powers, R. W. Gill, An axial velocity estimator for ultrasound blood flow imaging, based on a full evaluation of the doppler equation by means of a two-dimensional autocorrelation approach. *IEEE Trans. Ultrason. Ferroelectr. Freq. Control* **42**, 672–688 (1995).
49. T. J. Hall, M. Bilgen, M. F. Insana, T. A. Krouskop, Phantom materials for elastography. *IEEE Trans. Ultrason. Ferroelectr. Freq. Control* **44**, 1355–1365 (1997).
50. R. W. Ogden, Incremental Statics and Dynamics of Pre-Stressed Elastic Materials. *Waves in Nonlinear Pre-Stressed Materials*, M. Destrade, G. Saccomandi, Eds. (Springer, Vienna, 2007), vol. 495, pp. 1–26.
51. G.-Y. Li, Y. Zheng, Y. Liu, M. Destrade, Y. Cao, Elastic Cherenkov effects in transversely isotropic soft materials-I: Theoretical analysis, simulations and inverse method. *J. Mech. Phys. Solids* **96**, 388–410 (2016).
52. M. Destrade, M. D. Gilchrist, G. Saccomandi, Third- and fourth-order constants of incompressible soft solids and the acousto-elastic effect. *J. Acoust. Soc. Am.* **127**, 2759–2763 (2010).
53. I. Tsvankin, *Seismic signatures and analysis of reflection data in anisotropic media* (Society of Exploration Geophysicists, 2012).
54. G.-Y. Li, Z.-Y. Zhang, J. Qian, Y. Zheng, W. Liu, H. Wu, Y. Cao, Mechanical characterization of functionally graded soft materials with ultrasound elastography. *Philos. Trans. A. Math. Phys. Eng. Sci.* **377**, 20180075 (2019).
55. J. G. Murphy, Transversely isotropic biological, soft tissue must be modelled using both anisotropic invariants. *Eur. J. Mech. A/Solids* **42**, 90–96 (2013).

Acknowledgments
Funding: Y.C. acknowledges the support from the National Natural Science Foundation of China (grants nos. 11972206 and 11921002). A.L.G. is grateful for the support from the European Commission Horizon 2020/H2020 - Shift2Rail. M.D. acknowledges the support from the 111 Project for International Collaboration No. B21034 (Chinese Government, P.R. China), the Seagull Program (Zhejiang Province, P.R. China), the National Natural Science Foundation of China (no. 11872329), and the Natural Science Foundation of Zhejiang Province (no. LD21A020001). **Author contributions:** Y.C. and G.-Y.L. designed the research. Z.Z., G.-Y.L., Y.J., and Y.Z. performed the research. A.L.G. and M.D. contributed to the theoretical analysis. Z.Z., G.-Y.L., Y.J., Y.Z., and Y.C. analyzed the data. Z.Z., G.-Y.L., Y.C., A.L.G., and M.D. wrote the paper. **Competing interests:** Y.C., Z.Z., and Y.Z. are inventors on a patent application related to this work filed by Tsinghua University (no. 2022114284041, filed 15 November 2022). The authors declare that they have no other competing interests. **Data and materials availability:** All data needed to evaluate the conclusions in the paper are present in the paper and/or the Supplementary Materials.

Submitted 9 June 2022
Accepted 7 February 2023
Published 8 March 2023
10.1126/sciadv.add4082

Science Advances
AAAS

Supplementary Materials for

Noninvasive measurement of local stress inside soft materials with programmed shear waves

Zhaoyi Zhang *et al.*

Corresponding author: Yanping Cao, caoyanping@tsinghua.edu.cn; Guo-Yang Li, gli26@mgh.harvard.edu

Sci. Adv. **9**, eadd4082 (2023)
DOI: 10.1126/sciadv.add4082

The PDF file includes:

Other Supplementary Material for this manuscript includes the following:

Supplementary Note 1: The stress identity

Here we prove the following identity, used in the paper to connect wave speeds with stress:

$$\sigma_{11} - \sigma_{33} = \mathcal{A}^0_{1313} - \mathcal{A}^0_{3131}. \tag{S-1}$$

In the paper we write these moduli as $\alpha = \mathcal{A}^0_{1313}$ and $\gamma = \mathcal{A}^0_{3131}$, and considered scenarios where the components of the Cauchy stress σ_{11} and σ_{33} are the principal stresses σ_1 and σ_3, respectively. Here $\mathcal{A}^0_{piqj}$ are the Cartesian components of the Eulerian elasticity tensor. For incompressible solids, they are determined from the strain energy function W and the deformation gradient tensor with components F_{iJ} as (*28, 50*)

$$\mathcal{A}^0_{piqj} = (\sigma_{pq} + \bar{p}\delta_{pq})\delta_{ij} + 4F_{pP}F_{qQ}\frac{\partial^2 W}{\partial C_{IP}C_{QJ}}F_{iI}F_{jJ}, \tag{S-2}$$

where $C_{IJ} = F_{kI}F_{kJ}$, summation over repeated indices is implied, and δ_{ij} is the Kronecker delta. Hence

$$\mathcal{A}^0_{1313} = \sigma_{11} + \bar{p} + 4F_{1P}F_{1Q}\frac{\partial^2 W}{\partial C_{IP}C_{QJ}}F_{3I}F_{3J}, \tag{S-3}$$

$$\mathcal{A}^0_{3131} = \sigma_{33} + \bar{p} + 4F_{3P}F_{3Q}\frac{\partial^2 W}{\partial C_{IP}C_{QJ}}F_{1I}F_{1J} = \sigma_{33} + \bar{p} + 4F_{1P}F_{1Q}\frac{\partial^2 W}{\partial C_{IP}C_{QJ}}F_{3I}F_{3J}, \tag{S-4}$$

where for the last equation we swapped the dummy variables $I \leftrightarrow P$ and $Q \leftrightarrow J$, and then we used the symmetries $C_{IP} = C_{PI}$. By subtraction we obtain the identity (S-1).

Often the stress is modeled as being caused by a finite elastic deformation from a stress-free configuration. When instead, we consider small elastic waves in an initially stressed reference where the initial stress, denoted by τ_{ij} is due to *any origin*, then in the above we would take $F_{pP} = \delta_{pP}$ (*28, 29*), and the identity would still hold.

For future reference, we recall that the Cauchy stress is computed as (*50*)

$$\sigma_{ij} = F_{iK}\frac{\partial W}{\partial F_{jK}} - \bar{p}\delta_{ij}, \tag{S-5}$$

where $\bar{p}$ is a Lagrange multiplier due to the constraint of incompressibility.

Supplementary Note 2: Phase and group velocity

Here we relate the wave speeds to the moduli appearing in the stress identity (S-1).

We start with the equation of motion for plane shear waves of the form $\boldsymbol{u} = \boldsymbol{u}_0 e^{ik(\boldsymbol{n}\cdot\boldsymbol{x}-vt)}$, which is given by Equation (5.16) in Ref. (*51*):

$$(\boldsymbol{I} - \boldsymbol{n}\boldsymbol{n}^{\mathrm{T}})\boldsymbol{Q}(\boldsymbol{n})(\boldsymbol{I} - \boldsymbol{n}\boldsymbol{n}^{\mathrm{T}})\boldsymbol{u}_0 = \rho v^2 \boldsymbol{u}_0, \tag{S-6}$$

where $\boldsymbol{x} = (x_1, x_2, x_3)$, $\boldsymbol{n} = (n_1, n_2, n_3)$, $Q_{ij}(\boldsymbol{n}) = \mathcal{A}^0_{piqj} n_p n_q$, and $\boldsymbol{u}_0$ is a unit vector along the direction of polarization (orthogonal to $\boldsymbol{n}$, the unit vector along the direction of propagation). Then its wave speed v is given by

$$\rho v^2 = \boldsymbol{u}_0^{\mathrm{T}} \boldsymbol{Q}(\boldsymbol{n}) \boldsymbol{u}_0. \tag{S-7}$$

Let v_x and v_z be the speeds of the shear waves when $\boldsymbol{n} = (1, 0, 0)$, $\boldsymbol{u}_0 = (0, 0, 1)$, and $\boldsymbol{n} = (0, 0, 1)$, $\boldsymbol{u}_0 = (1, 0, 0)$, respectively. From the above it follows that

$$\rho v_x^2 = \mathcal{A}^0_{1313}, \qquad \rho v_z^2 = \mathcal{A}^0_{3131}. \tag{S-8}$$

To guarantee that there are two shear waves with speeds (S-8) that satisfy the equation of motion (S-6), we assume that all forms of anisotropy are coaxial with the deformation tensor $\boldsymbol{C} = \boldsymbol{F}\boldsymbol{F}^{\mathrm{T}}$. Different types of anisotropy, such as the ones captured by an initial stress tensor $\boldsymbol{\tau}$ (*28–30*) or a structural anisotropy tensor $\boldsymbol{M}\boldsymbol{M}^{\mathrm{T}}$ (where $\boldsymbol{M}$ is a unit vector along the preferred direction in the reference configuration for transversely isotropic materials, see for example Ref. (*51*)), can be included in the strain-energy W, from which we can deduce the moduli $\mathcal{A}^0_{piqj}$ with (S-2). For example, $\boldsymbol{\tau}$ and $\boldsymbol{M}\boldsymbol{M}^{\mathrm{T}}$ are coaxial with $\boldsymbol{C}$, and themselves, when

$$\boldsymbol{C}\boldsymbol{\tau} = \boldsymbol{\tau}\boldsymbol{C}, \quad \boldsymbol{C}\boldsymbol{M}\boldsymbol{M}^{\mathrm{T}} = \boldsymbol{M}\boldsymbol{M}^{\mathrm{T}}\boldsymbol{C}, \quad \text{and} \quad \boldsymbol{\tau}\boldsymbol{M}\boldsymbol{M}^{\mathrm{T}} = \boldsymbol{M}\boldsymbol{M}^{\mathrm{T}}\boldsymbol{\tau}.$$

This condition implies, for example, that $\boldsymbol{M}$ is aligned with the principal directions of the initial stress $\boldsymbol{\tau}$ and the final stress $\boldsymbol{\sigma}$.

In more detail, W can be written as a sum and multiplication of terms of the form tr $(\boldsymbol{A}\boldsymbol{C}^n\boldsymbol{B})$ for integer n where $\boldsymbol{A}$ and $\boldsymbol{B}$ are some multiplication of anisotropy tensors such as $\boldsymbol{\tau}$ and $\boldsymbol{M}\boldsymbol{M}^{\mathrm{T}}$. When all these tensors are coaxial, and we choose a coordinate system aligned with their axes, we find that

$$\mathcal{A}^0_{piqj} = 0 \quad \text{unless} \quad \begin{cases} p = i \;\&\; q = j, & \text{or} \\ p = q \;\&\; i = j, & \text{or} \\ p = j \;\&\; q = i. \end{cases} \tag{S-9}$$

By assuming the above, we can deduce which elastic shear waves can give us access to the stress identity (S-1).

Let $\boldsymbol{n} = (\cos\theta, \sin\theta, 0)$ and $\boldsymbol{u}_0 = (-\sin\theta, \cos\theta, 0)$, which substituted into (S-7) leads to

$$\rho v^2 = \alpha\cos^4\theta + 2\beta\cos^2\theta\sin^2\theta + \gamma\sin^4\theta, \tag{S-10}$$

where the moduli α, β, γ are defined as $\alpha = \mathcal{A}^0_{1313}$, $2\beta = \mathcal{A}^0_{1111} + \mathcal{A}^0_{3333} - 2\mathcal{A}^0_{1133} - 2\mathcal{A}^0_{3113}$, $\gamma = \mathcal{A}^0_{3131}$. Note this is the same result as deduced in (*25, 50, 52*) with the difference that here we showed that it holds in general when (S-9) holds. This justifies how and when our method applies to anisotropic solids under stress.

Now consider two shear waves, one with propagation direction $\theta = \theta_0$ and the other with $\theta = \pm\pi/2 \pm \theta_0$ with the speeds v_x and v_z, respectively. Then, according to Eq. (S-10) and (S-1), we find that

$$\sigma_1 - \sigma_3 = \rho\frac{v_x^2 - v_z^2}{\cos 2\theta_0}, \tag{S-11}$$

a generalization of the result established in (*25*) for isotropic solids.

The group velocities $\boldsymbol{v}_g$ are often easier to measure in shear wave elastography experiments, in comparison to the phase speed given by Eq. (S-10). The group velocity depends on the anisotropy of the material, and the initial forcing of the wave (*34*), what we call the Acoustic Radiation Force (ARF). For the ARF we programmed, as shown in Fig. 2 and Fig. S2, we were able to generate waves propagating along the x and z directions whose wavefronts are locally

flat. In these cases, the phase velocity can be measured, so in conclusion we can use Eq. (S-10). However, it is certainly easier to generate a point ARF. So we also discuss this case.

For an ARF focused on one point that equally excites bulk waves in all directions, the group velocity is given by $\boldsymbol{v}_g = \partial(kv)/\partial\boldsymbol{k}$ (*34*), where $\boldsymbol{k} = k\boldsymbol{n}$ denotes the wave vector. For the phase velocity v given by Eq. (S-10) we obtain the group velocities:

$$v_{g1} = \frac{\alpha\cos\theta + (2\beta - \alpha - \gamma)\sin^4\theta\cos\theta}{\rho v}, \tag{S-12}$$

and

$$v_{g3} = \frac{\gamma\sin\theta + (2\beta - \alpha - \gamma)\sin\theta\cos^4\theta}{\rho v}. \tag{S-13}$$

Equations (S-12) and (S-13) show that the phase and group speed are identical in the principal directions $\theta = 0$ and $\pi/2$, because there, $\rho v^2 = \alpha, \gamma$, respectively. The coincidence of the two speeds along and at the right angle to the axis of symmetry always holds, see (*53, p.16*) for example. For isotropic materials subject to moderate stress we have the further simplification $2\beta \approx \alpha + \gamma$ (*52*), which results in

$$\rho v^2 = \alpha\cos^2\theta + \gamma\sin^2\theta, \qquad v_{g1} = \frac{\alpha\cos\theta}{\rho v}, \qquad v_{g3} = \frac{\gamma\sin\theta}{\rho v}, \tag{S-14}$$

and thus

$$\frac{v_{g1}^2}{\alpha/\rho} + \frac{v_{g3}^2}{\gamma/\rho} = 1, \tag{S-15}$$

which describes an elliptical wavefront. This elliptical wavefront has also been revealed by Rouze et al. (*34*) in the case of the Mooney-Rivlin material, where $2\beta = \alpha + \gamma$ always holds regardless of the stress level. However, for other constitutive models such as the Arruda–Boyce model, Rouze et al. (*34*) show that cusp structures in wavefront may emerge in isotropic materials when sufficiently large stress is applied. These cusps are usually induced by structural anisotropy of materials, as shown in Fig. S1.

For experiments where only the group velocities are available (which is not our case), it would be necessary to first calculate the phase velocities from the measured group velocities.

Supplementary Note 3: Measurement of the lateral shear wave speed

We performed two-dimensional Fourier transforms on Fig. S4A to get the frequency-wavenumber domain data, as shown in Fig. S4B. To identify the left-to-right (LR) shear waves, we performed an inverse Fourier transform to the data in the first and third quadrants (and set the data points in the second and fourth quadrants to zero), as shown in Fig. S4C. Similarly, the right-to-left (RL) shear waves were obtained by inverse Fourier transform on the data in the second and fourth quadrants (Fig. S4D).

We then performed Radon transformations to the spatiotemporal data to obtain the shear wave group velocity. The Radon transform sums the intensity of pixels in a spatiotemporal map along projections with different slopes (denoted by $\tan\Theta$) and intercepts. The optimal projection is identified by the peak Radon sum (*41*). For the lateral shear waves, the six wavefronts induced by the six ARF pushes are parallel, resulting in multiple peaks in the Radon sum (Figs. S4E and F). Therefore, we summed the absolute values of the Radon sums obtained from the projections with the same slopes (each column of the Radon sums), as shown in Figs. S4G and H. We identified the maxima in Figs. S4G and H, respectively, to get the group velocities of the LR and RL shear waves, i.e., $\sim |\tan 67^\circ|\frac{\Delta x}{\Delta t}$ and $\sim |\tan 113^\circ|\frac{\Delta x}{\Delta t}$, respectively, where $\Delta x = 0.1$ mm and $\Delta t = 0.1$ ms are the grid size of spatiotemporal maps. Finally we reported the average of the two optical group velocities as the value of v_x.

Supplementary Note 4: Hydrogel sample characterization

The hydrogel consists of 10% polyvinyl alcohol (PVA), 3% cellulose and 87% deionized water by weights. We dissolved the PVA powder (sigma Aldrich 341584, Shanghai, China) into 80°C water. We then added cellulose powder (Sigma-Aldrich S3504, Shanghai, China) into the solution and fully stirred the solution to get a suspension of the cellulose powder. The cellulose particles act as ultrasonic scatterers to enhance the imaging contrast. We poured the suspension into a square plastic box (length ~ 30 cm, width ~ 7 cm, and height ~ 4 cm), and then cooled the suspension to room temperature (~ 20°C) before putting it into a −20°C freezer. We froze the sample for 12 hours and then thawed it at room temperature for another 12 hours. The stiffness of the sample can be tuned by the freezing/thawing (F/W) cycles (*49*). The hydrogel sample used in this study underwent two F/W cycles.

We performed indentation tests (Fig. S5A) to characterize the viscoelastic properties of the hydrogel sample. To get the long-term modulus, we performed three indentation tests using a low loading rate (~ 0.1 mm/s), as shown in Fig. S5B. The long-term shear modulus $\mu_\infty = \mu(t \to +\infty)$ can be obtained by fitting the loading curve with the formula

$$F = \frac{16}{9}\mu_\infty R^{1/2} h^{3/2}, \tag{S-16}$$

where $R \approx 7.5$ mm is the radius of the indenter, F is the force, and h is the indentation depth. As shown in Fig. S5B, the best fitting gives $\mu_\infty = 8.6 \pm 0.3$ kPa. We then increased the loading rate (~ 100 mm/s) and measured the stress relaxation when holding the indentation depth at ~ 5 mm. Figure S5C shows the normalized stress relaxation curve. We find the two-term Prony series with $g_1 = 0.07$, $\tau_1 = 0.08$ s, $g_2 = 0.05$ and $\tau_2 = 2.05$ s fits the stress relaxation data well. The total stress relaxation is small ($g_1 + g_2 \approx 10\%$), indicating a weak viscosity of the hydrogel sample, which only introduces a ~ 5% variation in shear wave speed over the frequency range from ~ 0.5 Hz (τ_2^{-1}) to ~ 12.5 Hz (τ_1^{-1}).

While the stress relaxation characterizes the viscoelasticity in the low frequency regime (below $\sim$ 12.5 Hz), we further measured the surface wave phase velocity up to 800 Hz using our ultrasound elastography system. In this measurement, we relied on a mechanical shaker (SA-JZ002, Shiao, Jiangsu, China) to apply a surface pressure locally to generate harmonic surface waves. The surface waves were acquired by the ultrasound transducer. We then computed the wavelengths of the surface waves to get the phase velocity. As shown in Fig. S5D, interestingly, we do not observe an increase in the speed, but instead a slight decrease. We attribute this decrease to the slight stiffness gradient (softer at shallower locations) of the hydrogel sample introduced by the fabrication process (*54*). Despite the slight material heterogeneity, the dispersion relation suggests a weak dependence of the surface wave speed on the frequency, indicating a weak viscosity of the hydrogel in the frequency range of 100 to 800 Hz.

Supplementary Note 5: Acoustoelastic model for skeletal muscle and the effect of viscoelasticity

Linear elastic parameters

To characterize the anisotropy of the skeletal muscle, we measured the shear wave group velocities along different directions. Our main assumption is that the skeletal muscle can be modeled as an incompressible transversely isotropic material due to a preferred direction of the muscle fibers. Such a material has three independent elastic parameters, say μ_T, the transverse shear modulus, μ_L, the longitudinal shear modulus, and E_L, the longitudinal Young modulus.

We measured the horizontal shear wave speeds v_x in the undeformed material at three different orientations of the fibers with respect to the x axis ($0, 35, 90°$, see Figs. S4a-c) to get $v_x^{0°}$, $v_x^{35°}$, and $v_x^{90°}$. Then the three elastic parameters can be calculated by the formulas (*51*)

$$\mu_T = \rho(v_x^{90°})^2, \quad \mu_L = \rho(v_x^{0°})^2, \quad E_L = \frac{4\left[\rho(v_x^{35°})^2 - \mu_L\right]}{\sin^2(2\times 35°)} + (4\mu_L - \mu_T). \tag{S-17}$$

Figure S6 shows the statistical results for the shear wave speeds, which clearly point to the mechanical anisotropy of the muscle. From the wave speeds we get $\mu_T \approx 10.7$ kPa, $\mu_L \approx 22.4$ kPa, and $E_L \approx 40.1$ kPa.

Acoustoelastic model for skeletal muscle

To model the acoustoelasticity of the skeletal muscle, we take the phenomenological model proposed by Murphy (*55*),

$$W = \frac{\mu_T}{2c_2}[e^{c_2(I_1-3)} - 1] + \frac{E_L + \mu_T - 4\mu_L}{2c_4}[e^{c_4(\sqrt{I_4}-3)} - 1] + \frac{\mu_T - \mu_L}{2}(2I_4 - I_5 - 1), \tag{S-18}$$

where c_2 and c_4 are non-dimensional strain-hardening parameters, and the strain invariants are defined as

$$I_1 = \operatorname{tr}\boldsymbol{C}, \qquad I_2 = \tfrac{1}{2}[I_1^2 - \operatorname{tr}(\boldsymbol{C}^2)], \qquad I_4 = \boldsymbol{M}\cdot(\boldsymbol{C}\boldsymbol{M}), \qquad I_5 = \boldsymbol{M}\cdot(\boldsymbol{C}^2\boldsymbol{M}). \tag{S-19}$$

This model reduces to the neo-Hookean model,

$$W = \mu(I_1 - 3), \tag{S-20}$$

when we take $\mu_T = \mu_L = \frac{1}{3}E_L = \mu$ and $c_2 = 0$.

Inserting (S-18) into (S-2) we obtain the expressions for α, β, and γ, which determine the shear wave speed according to Eq. (1) in the main text. When $\boldsymbol{M} = (1, 0, 0)$, we find

$$\begin{aligned}\rho v^2 = {} & \mu_T \lambda^2 \sin^2\theta e^{c_2(I_1-3)} + \lambda^{-1}\cos^2\theta\left[\mu_T e^{c_2(I_1-3)} + (\mu_T - \mu_L)(2 - 3\lambda^{-1})\right] \\ & + \lambda^{-1}\cos^2\theta\left[(E_L + \mu_T - 4\mu_L)e^{c_4(\lambda-1)^2}(1 - \lambda^{-1})\right],\end{aligned} \tag{S-21}$$

where $I_1 = \lambda^2 + 2\lambda^{-1}$, and λ is the stretch ratio along the direction of tension, obtained by solving

$$\begin{aligned}\sigma_1 = {} & \lambda\left[\mu_T\lambda e^{c_2(I_1-3)} + (E_L + \mu_T - 4\mu_L)(\lambda - 1)e^{c_4(\lambda-1)^2} + 2(\mu_T - \mu_L)(\lambda - \lambda^3)\right] \\ & - \frac{\mu_T}{\lambda}e^{c_2(I_1-3)},\end{aligned} \tag{S-22}$$

given the principal stress σ_1. Figure S1 shows the typical dependence of the wave speed on direction when the material is subject to a uni-axial tension.

Inserting $\mu_T = 10.7$ kPa, $\mu_L = 22.4$ kPa, and $E_L = 40.1$ kPa into Eq. (S-21), and then using this equation to fit $v_x(\theta = 0)$ and $v_z(\theta = \pi/2)$ shown in Fig. 4d, we get $c_2 \approx 3.5$ and $c_4 \approx 8$. The fitting curves are shown in Fig. 4d of the main text.

Viscoelasticity of the skeletal muscle and its effect on shear wave propagation

The dispersion relation of the Rayleigh surface wave in the muscle sample was measured using the same setup as described in Note 4. Figure S4E shows the surface wave speeds measured along the muscle fiber. We fit the dispersion relation with a one-term Prony series, to get $g_1 \approx 0.79$ and $\tau_1 \approx 0.49$ ms.

To evaluate the effect of the viscoelasticity on the acoustoelastic imaging, we use the acousto-visco-elastic model recently proposed by Berjamin and de Pascalis (*46*). For simplicity, we

consider the quasi-linear viscoelasticity (QLV) theory with the neo-Hookean model (Eq. (S-20)) and a one-term Prony series. According to (*46*), the shear wave speed v_x is a function of the frequency f,

$$v_x = \sqrt{\frac{2(1+D^2)}{1+\sqrt{1+D^2}}}\sqrt{\frac{|\mathrm{Re}\,\mu_x|}{\rho}} \tag{S-23}$$

where

$$\begin{aligned} D &= D_0\frac{2\Omega\Omega_0}{\Omega^2+\Omega_0^2}, \qquad \Omega = 2\pi f\tau_1, \\ D_0 &= \frac{g}{2\Omega_0}\frac{\bar{\mu}_x^{\mathrm{v}}}{\bar{\mu}_x^{\mathrm{v}}+(1-g)[\bar{T}_{\mathrm{d}}^{\mathrm{e}}]_{11}}, \qquad \Omega_0^2 = (1-g)\frac{\bar{\mu}_x^{\mathrm{v}}+[\bar{T}_{\mathrm{d}}^{\mathrm{e}}]_{11}}{\bar{\mu}_x^{\mathrm{v}}+(1-g)[\bar{T}_{\mathrm{d}}^{\mathrm{e}}]_{11}}, \end{aligned} \tag{S-24}$$

and

$$\mu_x = (1-g_1)[\bar{T}_{\mathrm{d}}^{\mathrm{e}}]_{11} + (1-\frac{g_1}{1+i\omega\tau_1})\bar{\mu}_x^{\mathrm{v}}. \tag{S-25}$$

In (S-24) and (S-25), $i = \sqrt{-1}$,

$$[\bar{T}_{\mathrm{d}}^{\mathrm{e}}]_{11} = \mu(\lambda^2 - I_1/3), \qquad \bar{\mu}_x^{\mathrm{v}} = \mu I_1/3. \tag{S-26}$$

and λ is the stretch ratio, which can be determined from the stress σ_1 by solving the cubic

$$\lambda^3 - \frac{\sigma_1}{\mu_\infty}\lambda - 1 = 0, \tag{S-27}$$

where $\mu_\infty = \mu(\infty) = (1-g_1)\mu_0$ is the long-term shear modulus and $I_1 = \lambda^2 + 2\lambda^{-1}$. To get v_z, we follow the same procedure, replacing λ with $\lambda^{-1/2}$ in (S-26).

In Fig. S7, we plot the dispersion relations of v_x and v_z with $\mu_\infty = 8.4$ kPa, $g_1 = 0.79$ and $\tau_1 = 0.49$ ms. Then we use Eq. (2) in the main text to derive the stress σ_1. As shown in Fig. S7B, the stress is underestimated when the viscoelasticity comes into play.

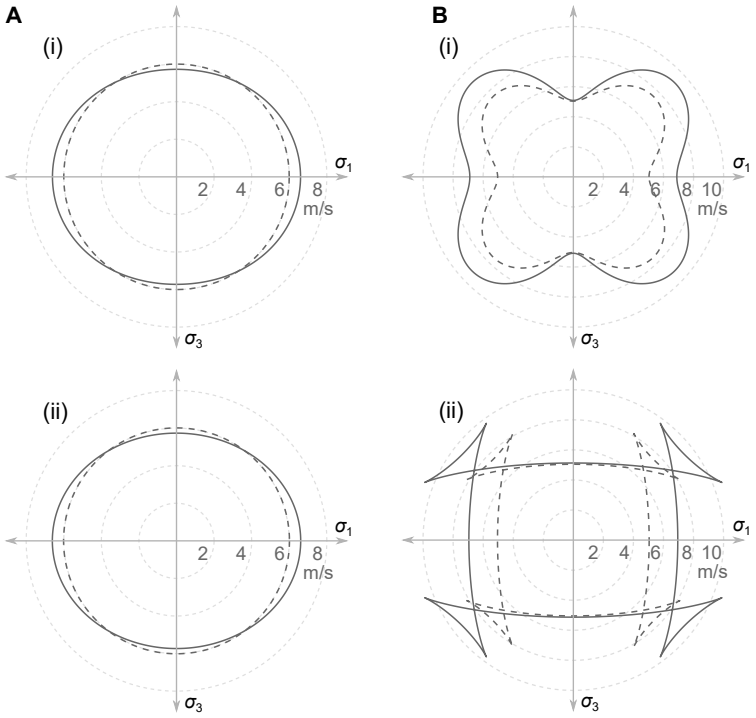

Fig. S1: **Effect of the uniaxial stress on the shear wave speeds.** (**A**) neo-Hookean material with shear modulus $\mu = 36$ kPa, subject to uniaxial stress $\sigma_1 = 0.3\mu$. (**B**) Transversely isotropic material with material parameters $\mu_T = 9$ kPa, $\mu_L = 25$ kPa, $E_L = 216$ kPa, $c_1 = 1$, $c_2 = 10$, and $\sigma_1/E_L = 0.1$. The fiber direction is aligned with x_1. (i) and (ii) depict phase and group speeds, respectively, showing that they are the same along the principal axes. Solid lines: prestressed. Dashed lines: stress-free.

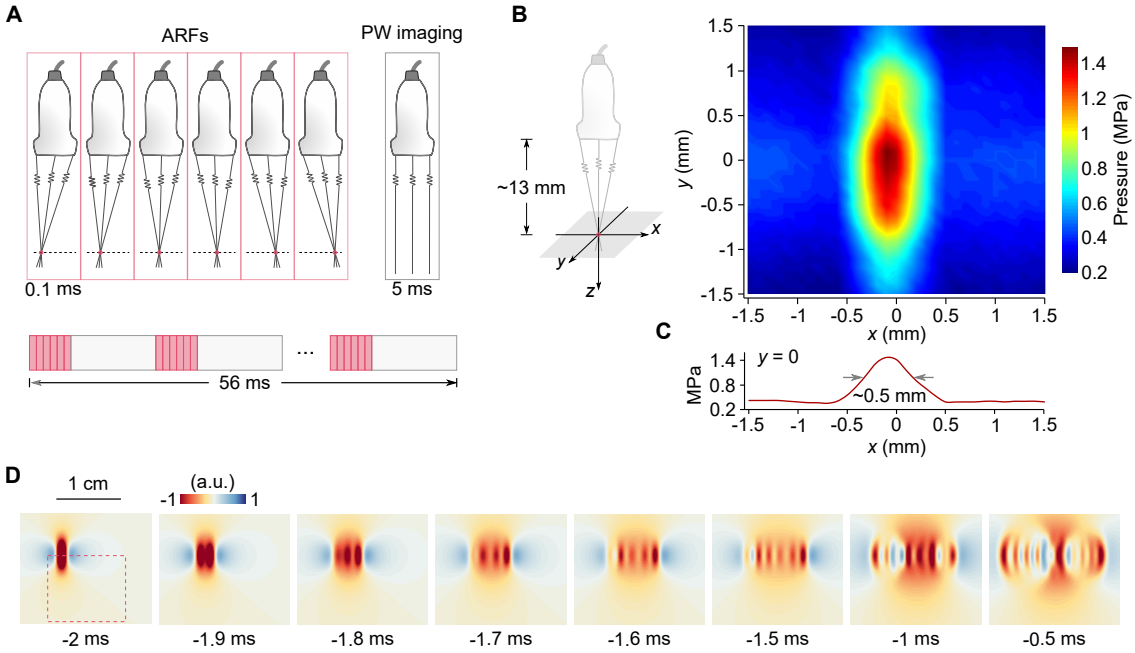

Fig. S2: **Imaging protocol and finite element simulation of shear wave excitation.** (**A**) Imaging protocol. Six ARFs are applied by successively focusing the ultrasound beam along the horizontal direction. The duration of each ARF is ~ 0.1 ms. After the excitation (~ 0.6 ms), the transducer is switched to perform plane wave (PW) imaging (unfocused beam, duration 5 ms) at a frame rate of 10 kHz. Ten successive measurements (~ 56 ms) are performed and then the average of the measurements is taken to improve the signal-to-noise ratio. (**B**) Acoustic pressure of the focused ultrasound beam measured within the focal plane (~ 13 mm away from the transducer). (**C**) Distribution of the pressure along x axis. Half width at half maximum (HWHM) is approximately ~ 0.25 mm, in agreement with the ultrasound wavelength ~ 0.23 mm. (**D**) Finite element simulations showing the six ARFs successively applied to excite the shear waves. The time when the PW imaging starts is set to 0. The dashed square shows the region of interest where the wave propagation is measured by the PW imaging.

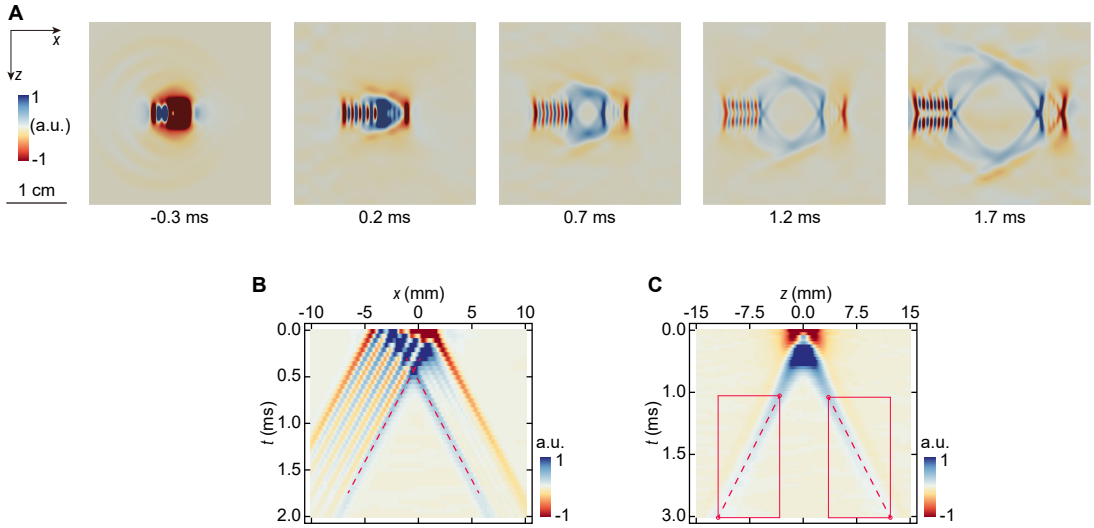

Fig. S3: **Finite element simulation of the shear wave excitation by programmed acoustic radiation forces in anisotropic materials.** (**A**) The snapshots of the shear wave propagation, which suggest the SV shear waves are primarily excited. The maps depict the vertical particle velocity fields. (**B**) and (**C**) Spatiotemporal data for the horizontal and vertical waves, respectively. The speeds measured along the two directions are identical, $\sim$ 4.7 m/s ($\sqrt{\mu_L/\rho}$), indicating the SV shear waves are measured in both directions. The material is incompressible transversely isotropic. The fiber direction is aligned with x. The material parameters used in the simulation are μ_T = 10.7 kPa, μ_L = 22.4 kPa, E_L = 40.1 kPa, and ρ = 1000 kg/m^3 (see Note 5 for definitions of the material parameters).

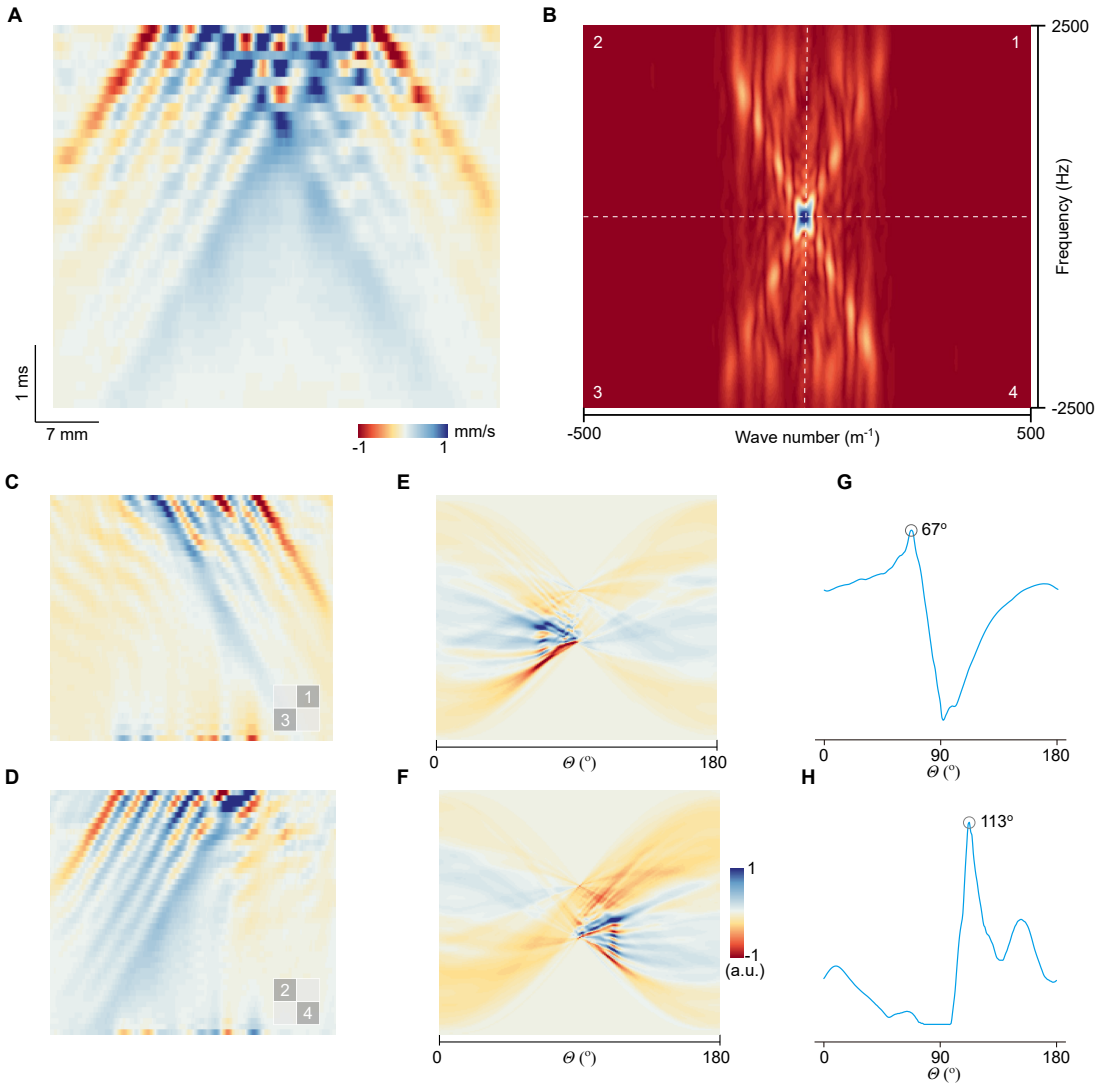

Fig. S4: **Measurement of the lateral shear wave speed v_x.** (**A**) Spatiotemporal map of the shear waves propagating along the horizontal direction (x axis). (**B**) Fourier transformation of the spatiotemporal data. (**C**) Inverse Fourier transformation of the data in the first and third quadrants. The right-to-left (RL) waves have been filtered out in this map. (**D**) Inverse Fourier transformation of the data in the second and fourth quadrants. The left-to-right (LR) waves have been filtered out in this map. (**E**) and (**F**) The Radon transformations of (**C**) and (**D**). Then We sum the absolute values of the data points in (**E**) and (**F**) along each column to get the solid lines in (**G**) and (**H**), respectively. The peaks identified on the lines give the optimal phase velocities of the LR and RL waves.

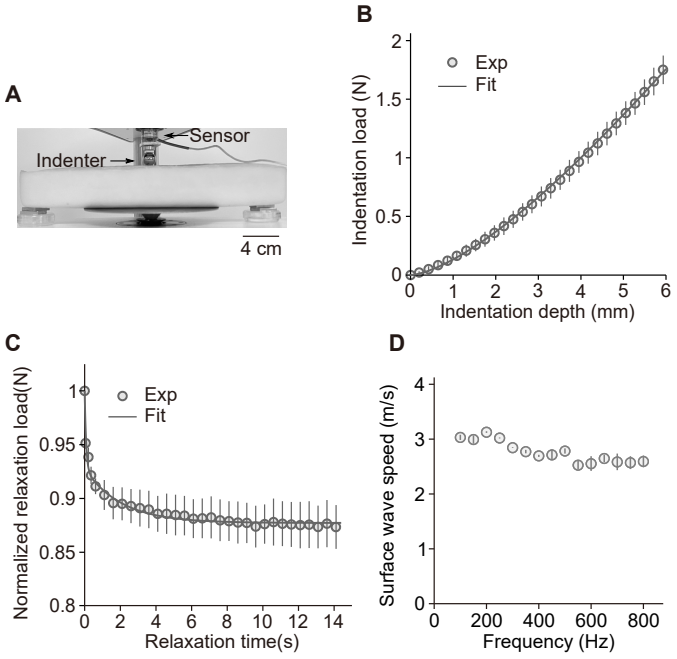

Fig. S5: **Mechanical characterization of the hydrogel phantom at rest.** (**A**) Photography showing the indentation tests on the hydrogel phantom. (**B**) Load-displacement curve of the indentation experiments obtained from the loading process with a low loading rate (~ 0.1 mm/s). Error bar, standard deviations over five measurements. (**C**) Normalized stress relaxation curve. Error bar: standard deviations over ten measurements. (**D**) Phase velocity of the surface waves.

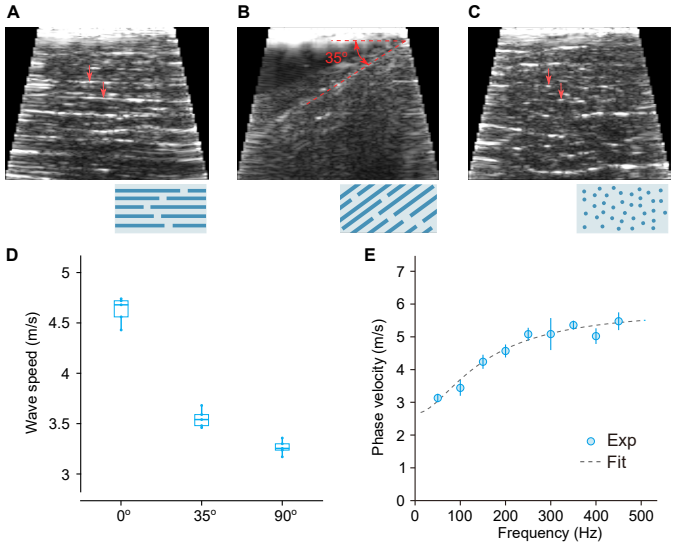

Fig. S6: **Mechanical characterization of the skeletal muscle at rest.** (**A**)-(**C**) Grayscale ultrasound images of the skeletal muscle. Red arrows in (**A**) and (**C**) indicate some of the parallel muscle fibers. For (**B**) the sample is tilted at $\sim 35°$. The schematics underneath each image show the orientations of the muscle fibers. For all three cases, the horizontal shear wave group velocities v_x are measured. Therefore, the angles between the shear wave propagation direction and muscle fibers are (**A**) 0°, (**B**) 35°, and (**C**) 90°. (**D**) Statistical results (five independent measurements) for the horizontal shear wave group velocities. (**E**) Dispersion relation of the surface waves (0°). Markers, experiments. Dashed line, fitting curve obtained using one-term Prony series with $g_1 = 0.79$ and $\tau_1 = 0.49$ ms.

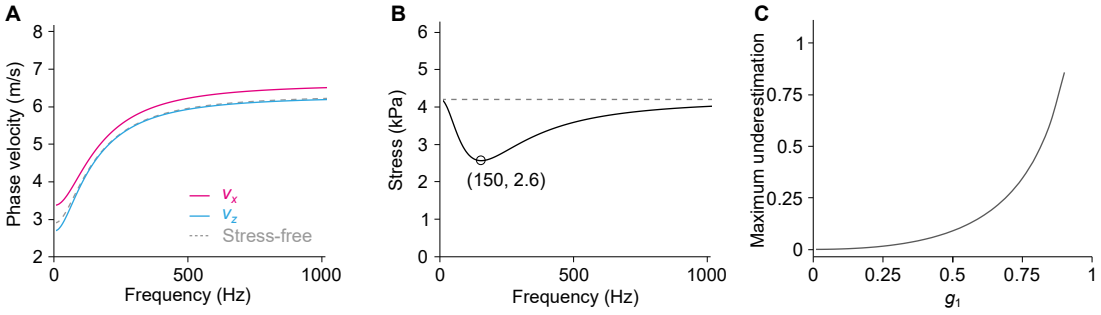

Fig. S7: **Effect of viscoelasticity on the acoustoelastic imaging.** (**A**) Dispersion relations of v_x and v_z when a tensile stress $\sigma_1 = 4.2$ kPa is applied. The dashed curve is the dispersion relation in the stress free state. The Quasi-Linear Viscoelastic material model used to produce this figure relies on the neo-Hookean model with $\mu_0 = 40$ kPa and the one-term Prony series with $g_1 = 0.79$ and $\tau = 0.49$ ms. (**B**) The stresses derived from v_x and v_z at different frequencies. The minimum stress is 2.6 kPa, indicating an underestimation of $\sim 38\%$. (**C**) The underestimation of the stress as a function of g_1.

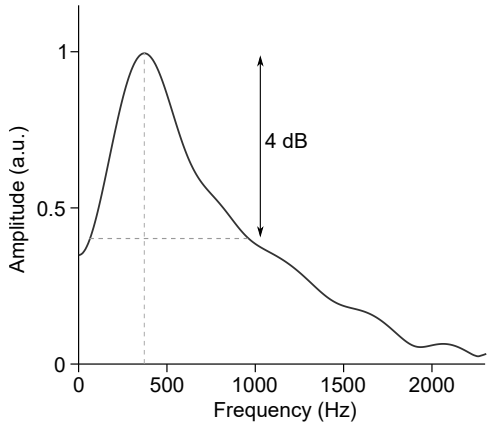

Fig. S8: **A representative spectrum of the shear waves in the muscle sample.** The central frequency is about 380 Hz and the 4dB bandwidth is about from 100 to 1,000 Hz.

Movie S1 (separate file). A movie given by finite element (FE) simulations compares the shear waves generated by programmed acoustic radiation force (ARF) and the conventional single ARF. (A) FE results of the shear waves generated by the programmed ARF; (B) FE results of the shear waves gener-ated by a single ARF.

Movie S2 (separate file). A movie compares the shear waves generated in experiments by the programmed ARF and the conventional single ARF. (A) Experimental measurements of the shear waves generated by the programmed ARF; (B) Experimental measurements of the shear waves generated by a single ARF.

REFERENCES AND NOTES

1. N. L. Nerurkar, C. Lee, L. Mahadevan, C. J. Tabin, Molecular control of macroscopic forces drives formation of the vertebrate hindgut. *Nature* **565**, 480–484 (2019).

2. M. Gómez-González, E. Latorre, M. Arroyo, X. Trepat, Measuring mechanical stress in living tissues. *Nat. Rev. Phys.* **2**, 300–317 (2020).

3. K. H. Vining, D. J. Mooney, Mechanical forces direct stem cell behaviour in development and regeneration. *Nat. Rev. Mol. Cell Biol.* **18**, 728–742 (2017).

4. H. Ucar, S. Watanabe, J. Noguchi, Y. Morimoto, Y. Iino, S. Yagishita, N. Takahashi, H. Kasai, Mechanical actions of dendritic-spine enlargement on presynaptic exocytosis. *Nature* **600**, 686–689 (2021).

5. T. Tallinen, J. Y. Chung, F. Rousseau, N. Girard, J. Lefèvre, L. Mahadevan, On the growth and form of cortical convolutions. *Nat. Phys.* **12**, 588–593 (2016).

6. J.-H. Lee, H. S. Park, D. P. Holmes, Elastic instabilities govern the morphogenesis of the optic cup. *Phys. Rev. Lett.* **127**, 138102 (2021).

7. B. Li, F. Jia, Y.-P. Cao, X.-Q. Feng, H. Gao, Surface wrinkling patterns on a core-shell soft sphere. *Phys. Rev. Lett.* **106**, 234301 (2011).

8. S. K. Powers, M. J. Jackson, Exercise-induced oxidative stress: Cellular mechanisms and impact on muscle force production. *Physiol. Rev.* **88**, 1243–1276 (2008).

9. J. A. Martin, S. C. Brandon, E. M. Keuler, J. R. Hermus, A. C. Ehlers, D. J. Segalman, M. S. Allen, D. G. Thelen, Gauging force by tapping tendons. *Nat. Commun.* **9**, 1592(2018).

10. J. Lee, S. J. Ihle, G. S. Pellegrino, H. Kim, J. Yea, C. Y. Jeon, H. C. Son, C. Jin, D. Eberli, F. Schmid, B. L. Zambrano, A. F. Renz, C. Forró, H. Choi, K. I. Jang, R. Küng, J. Vörös, Stretchable and suturable fibre sensors for wireless monitoring of connective tissue strain. *Nat. Electron.* **4**, 291–301 (2021).

11. J. Y. Sun, X. Zhao, W. R. Illeperuma, O. Chaudhuri, K. H. Oh, D. J. Mooney, J. J. Vlassak, Z. Suo, Highly stretchable and tough hydrogels. *Nature* **489**, 133–136 (2012).

12. J. Kim, G. Zhang, M. Shi, Z. Suo, Fracture, fatigue, and friction of polymers in which entanglements greatly outnumber cross-links. *Science* **374**, 212–216 (2021).

13. N. Matsuhisa, S. Niu, S. J. K. O'Neill, J. Kang, Y. Ochiai, T. Katsumata, H.-C. Wu, M. Ashizawa, G.-J. N. Wang, D. Zhong, X. Wang, X. Gong, R. Ning, H. Gong, I. You, Y. Zheng, Z. Zhang, J. B.-H. Tok, X. Chen, Z. Bao, High-frequency and intrinsically stretchable polymer diodes. *Nature* **600**, 246–252 (2021).

14. G. H. Lee, H. Moon, H. Kim, G. H. Lee, W. Kwon, S. Yoo, D. Myung, S. H. Yun, Z. Bao, S. K. Hahn, Multifunctional materials for implantable and wearable photonic healthcare devices. *Nat. Rev. Mater.* **5**, 149–165 (2020).

15. R. Bai, J. Yang, Z. Suo, Fatigue of hydrogels. *Eur. J. Mech. A/Solids* **74**, 337–370 (2019).

16. J. A. Rogers, T. Someya, Y. Huang, Materials and mechanics for stretchable electronics. *Science* **327**, 1603–1607 (2010).

17. Y. Wang, S. Lee, T. Yokota, H. Wang, Z. Jiang, J. Wang, M. Koizumi, T. Someya, A durable nanomesh on-skin strain gauge for natural skin motion monitoring with minimum mechanical constraints. *Sci. Adv.* **6**, eabb7043 (2020).

18. G. S. Schajer, Hole-drilling residual stress measurements at 75: Origins, advances, opportunities. *Exp. Mech.* **50**, 245–253 (2009).

19. N. S. Rossini, M. Dassisti, K. Y. Benyounis, A. G. Olabi, Methods of measuring residual stresses in components. *Mater. Des.* **35**, 572–588 (2012).

20. C. O. Ruud, A review of selected non-destructive methods for residual stress measurement. *NDT Int.* **15**, 15–23 (1982).

21. D. S. Hughes, J. L. Kelly, Second-order elastic deformation of solids. *Phys. Rev.* **92**, 1145 (1953).

22. A. N. Guz, F. G. Makhort, The physical fundamentals of the ultrasonic nondestructive stress analysis of solids. *Int. Appl. Mech.* **36**, 1119–1149 (2000).

23. F. Shi, J. E. Michaels, S. J. Lee, In situ estimation of applied biaxial loads with Lamb waves. *J. Acoust. Soc. Am.* **133**, 677–687 (2013).

24. J.-L. Gennisson, M. Rénier, S. Catheline, C. Barrière, J. Bercoff, M. Tanter, M. Fink, Acoustoelasticity in soft solids: Assessment of the nonlinear shear modulus with the acoustic radiation force. *J. Acoust. Soc. Am.* **122**, 3211–3219 (2007).

25. G.-Y. Li, A. Gower, M. Destrade, An ultrasonic method to measure stress without calibration: The angled shear wave method. *J. Acoust. Soc. Am.* **148**, 3963 (2020).

26. Y. Jiang, G. Y. Li, L. X. Qian, X. D. Hu, D. Liu, S. Liang, Y. Cao, Characterization of the nonlinear elastic properties of soft tissues using the supersonic shear imaging (SSI) technique: Inverse method, ex vivo and in vivo experiments. *Med. Image Anal.* **20**, 97–111 (2015).

27. C. Creton, C. Matteo, Fracture and adhesion of soft materials: A review. *Rep. Prog. Phys.* **79**, 046601 (2016).

28. M. Shams, M. Destrade, R. W. Ogden, Initial stresses in elastic solids: Constitutive laws and acoustoelasticity. *Wave Motion* **48**, 552–567 (2011).

29. A. L. Gower, T. Shearer, P. Ciarletta, A new restriction for initially stressed elastic solids. *Q. J. Mech. Appl. Math.* **70**, 455–478 (2017).

30. M. Destrade, M. D. Gilchrist, R. W. Ogden, Third-and fourth-order elasticities of biological soft tissues. *J. Acoust. Soc. Am.* **127**, 2103–2109 (2010).

31. C. Deroy, M. Destrade, A. Mc Alinden, A. Ní Annaidh, Non-invasive evaluation of skin tension lines with elastic waves. *Skin Res. Technol.* **23**, 326–335 (2017).

32. I. Hariton, G. Debotton, T. C. Gasser, G. A. Holzapfel, Stress-driven collagen fiber remodeling in arterial walls. *Biomech. Model. Mechanobiol.* **6**, 163–175 (2007).

33. G. W. Jones, S. J. Chapman, Modeling growth in biological materials. *SIAM Rev.* **54**, 52–118 (2012).

34. N. C. Rouze, A. Caenen, K. R. Nightingale, Phase and group velocities for shear wave propagation in an incompressible, hyperelastic material with uniaxial stretch. *Phys. Med. Biol.* **67**, 095015 (2022).

35. J. Bercoff, M. Tanter, M. Fink, Supersonic shear imaging: A new technique for soft tissue elasticity mapping. *IEEE Trans. Ultrason. Ferroelectr. Freq. Control* **51**, 396–409 (2004).

36. A. P. Sarvazyan, O. V. Rudenko, S. D. Swanson, J. B. Fowlkes, S. Y. Emelianov, Shear wave elasticity imaging: A new ultrasonic technology of medical diagnostics. *Ultrasound Med. Biol.* **24**, 1419–1435 (1998).

37. S. Catheline, N. Benech, Longitudinal shear wave and transverse dilatational wave in solids. *J. Acoust. Soc. Am.* **137**, EL200–EL205 (2015).

38. L. Sandrin, M. Tanter, J.-L. Gennisson, S. Catheline, M. Fink, Shear elasticity probe for soft tissues with 1-d transient elastography. *IEEE Trans. Ultrason. Ferroelectr. Freq. Control* **49**, 436–446 (2002).

39. L. Sandrin, D. Cassereau, M. Fink, The role of the coupling term in transient elastography. *J. Acoust. Soc. Am.* **115**, 73–83 (2004).

40. M. Tanter, M. Fink, Ultrafast imaging in biomedical ultrasound. *IEEE Trans. Ultrason. Ferroelectr. Freq. Control* **61**, 102–119 (2014).

41. N. C. Rouze, M. H. Wang, M. L. Palmeri, K. R. Nightingale, Robust estimation of time-of-flight shear wave speed using a radon sum transformation. *IEEE Trans. Ultrason. Ferroelectr. Freq. Control* **57**, 2662–2670 (2010).

42. J. P. Kerris, A. C. Betik, J. Li, G. K. McConell, Passive stretch regulates skeletal muscle glucose uptake independent of nitric oxide synthase. *J. Appl. Physiol.* **126**, 239–245 (2019).

43. B. Calvo, A. Ramírez, A. Alonso, J. Grasa, F. Soteras, R. Osta, M. J. Muñoz, Passive nonlinear elastic behaviour of skeletal muscle: Experimental results and model formulation. *J. Biomech.* **43**, 318–325 (2010).

44. J. P. Remeniéras, M. Bulot, J. L. Gennisson, F. Patat, M. Destrade, G. Bacle, Acousto-elasticity of transversely isotropic incompressible soft tissues: Characterization of skeletal striated muscle. *Phys. Med. Biol.* **66**, 145009 (2021).

45. A. E. Knight, C. A. Trutna, N. C. Rouze, L. D. Hobson-Webb, A. Caenen, F. Q. Jin, M. L. Palmeri, K. R. Nightingale, Full characterization of in vivo muscle as an elastic, incompressible, transversely isotropic material using ultrasonic rotational 3D shear wave elasticity imaging. *IEEE Trans. Med. Imag.* **41**, 133–144 (2021).

46. H. Berjamin, R. De Pascalis, Acoustoelastic analysis of soft viscoelastic solids with application to pre-stressed phononic crystals. *Int. J. Solids Struct.* **241**, 111529 (2022).

47. G. Montaldo, M. Tanter, J. Bercoff, N. Benech, M. Fink, Coherent plane-wave compounding for very high frame rate ultrasonography and transient elastography. *IEEE Trans. Ultrason. Ferroelectr. Freq. Control* **56**, 489–506 (2009).

48. T. Loupas, J. Powers, R. W. Gill, An axial velocity estimator for ultrasound blood flow imaging, based on a full evaluation of the doppler equation by means of a two-dimensional autocorrelation approach. *IEEE Trans. Ultrason. Ferroelectr. Freq. Control* **42**, 672–688 (1995).

49. T. J. Hall, M. Bilgen, M. F. Insana, T. A. Krouskop, Phantom materials for elastography. *IEEE Trans. Ultrason. Ferroelectr. Freq. Control* **44**, 1355–1365 (1997).

50. R. W. Ogden, Incremental Statics and Dynamics of Pre-Stressed Elastic Materials. *Waves in Nonlinear Pre-Stressed Materials*, M. Destrade, G. Saccomandi, Eds. (Springer, Vienna, 2007), vol. 495, pp. 1–26.

51. G.-Y. Li, Y. Zheng, Y. Liu, M. Destrade, Y. Cao, Elastic Cherenkov effects in transversely isotropic soft materials-I: Theoretical analysis, simulations and inverse method. *J. Mech. Phys. Solids* **96**, 388–410 (2016).

52. M. Destrade, M. D. Gilchrist, G. Saccomandi, Third- and fourth-order constants of incompressible soft solids and the acousto-elastic effect. *J. Acoust. Soc. Am.* **127**, 2759–2763 (2010).

53. I. Tsvankin, *Seismic signatures and analysis of reflection data in anisotropic media* (Society of Exploration Geophysicists, 2012).

54. G.-Y. Li, Z.-Y. Zhang, J. Qian, Y. Zheng, W. Liu, H. Wu, Y. Cao, Mechanical characterization of functionally graded soft materials with ultrasound elastography. *Philos. Trans. A. Math. Phys. Eng. Sci.* **377**, 20180075 (2019).

55. J. G. Murphy, Transversely isotropic biological, soft tissue must be modelled using both anisotropic invariants. *Eur. J. Mech. A/Solids* **42**, 90–96 (2013).